



ELSEVIER

Available online at www.sciencedirect.com ScienceDirect

Proceedings of the Combustion Institute xxx (2010) xxx–xxx

**Proceedings
of the
Combustion
Institute**www.elsevier.com/locate/proci

Large eddy simulation/probability density function modeling of a turbulent CH₄/H₂/N₂ jet flame

Haifeng Wang^{*}, Stephen B. Pope*Sibley School of Mechanical and Aerospace Engineering, Cornell University, Ithaca, NY 14853, USA*

Abstract

In this work, we develop the large-eddy simulation (LES)/probability density function (PDF) simulation capability for turbulent combustion and apply it to a turbulent CH₄/H₂/N₂ jet flame (DLR Flame A). The PDF code is verified to be second-order accurate with respect to the time-step size and the grid size in a manufactured one-dimensional test case. Three grids (64 × 64 × 16, 192 × 192 × 48, 320 × 320 × 80) are used in the simulations of DLR Flame A to examine the effect of the grid resolution. The numerical solutions of the resolved mixture fraction, the mixture fraction squared, and the density are duplicated in the LES code and the PDF code to explore the numerical consistency between them. A single laminar flamelet profile is used to reduce the computational cost of treating the chemical reactions of the particles. The sensitivity of the LES results to the time-step size is explored. Both first and second-order time splitting schemes are used for integrating the stochastic differential equations for the particles, and these are compared in the jet flame simulations. The numerical results are found to be sensitive to the grid resolution, and the 192 × 192 × 48 grid is adequate to capture the main flow fields of interest for this study. The numerical consistency between LES and PDF is confirmed by the small difference between their numerical predictions. Overall good agreement between the LES/PDF predictions and the experimental data is observed for the resolved flow fields and the composition fields, including for the mass fractions of the minor species and NO. The LES results are found to be insensitive to the time-step size for this particular flame. The first-order splitting scheme performs as well as the second-order splitting scheme in predicting the resolved mean and rms mixture fraction and the density for this flame.

© 2010 The Combustion Institute. Published by Elsevier Inc. All rights reserved.

Keywords: Large eddy simulation; Probability density function methods; Turbulent jet flame

1. Introduction

With the rapid development of modern high-performance computing technologies, numerical simulations of turbulent reactive flows have

become a major approach to understanding fundamental phenomena of turbulence, combustion and their strong interactions. Three levels of numerical simulations exist for turbulent combustion: direct numerical simulation (DNS); large-eddy simulation (LES); and Reynolds averaged Navier–Stokes simulation (RANS). DNS resolves all scales, and hence requires the most computer resources that are currently prohibitive for a high-Reynolds number turbulent combustion problem. RANS models turbulence at all scales

^{*} Corresponding author. Address: 245 Upson Hall, Cornell University, Ithaca, NY 14853, USA. Fax: +1 607 255 1222.

E-mail address: hw98@cornell.edu (H. Wang).

and has the least requirement of resolution and computer resources. LES resolves the large scales of turbulence, with the small scales being modeled, which poses an intermediate requirement for resolution and computer resources between DNS and RANS. Since the late 1990s, LES has become accessible to more and more studies and is likely to be a dominant methodology for the study of turbulence and turbulent combustion for a few decades to come.

In the LES of low-Mach number turbulent reactive flows, closure is required for chemical reactions due to their small scales compared to the turbulence resolution length scale, in addition to the closure requirements for the residual stress and scalar flux. A few promising closure models for sub-grid scale (SGS) combustion have emerged over the last 20 years, mostly derived directly from the models used in the RANS context, e.g., the laminar flamelet models [1], the conditional moment closure (CMC) [2,3], and the probability density function (PDF) methods [4–6]. PDF methods [7] have proved to be most successful in predicting turbulence-chemistry interactions in both RANS (e.g., [8,9]) and LES (e.g., [10,11]). The analogue of PDF in LES is often called filtered-density function (FDF) [4] defined based on the filtering operation normally used in LES. Different FDF approaches have been developed in the past, e.g., the composition FDF [6], the velocity-composition joint FDF [12] etc. The LES-FDF approaches have been employed in several previous studies of turbulent combustion, e.g., [10,11]. There are different viewpoints of the PDF used in LES, in addition to FDF. Fox [13] defined it as a conditional PDF (conditioned on resolved quantities). Recently, Pope [14] developed an alternative foundation for LES of turbulent flows based on self-conditioned fields, rather than on filtering. In this framework, it is the self-conditioned PDF that is defined to describe the residual fluctuations. Several advantages are provided by this method over the traditional LES as illustrated in [14]. In this work, we follow this new framework and use the terminology PDF instead of FDF. Practically, different methods of LES and PDF do not lead to substantially different partial differential equations to be solved. In fact the particle equations to solve arising from the current PDF framework are the same as those in the FDF method [4,6]. At this stage of development, the PDF and FDF are different only on the conceptual level [14]. Meanwhile, almost all models and algorithms for the PDF methods developed in the RANS context can be applied directly in LES.

An important task in advancing PDF methods in the LES context is to develop efficient and accurate algorithms and codes for practical applications. Although the LES/PDF (or LES/FDF) method has been implemented in several previous

works (e.g., [6,10,11]), solving the PDF equations accurately still remains to be investigated and validated in the context of LES. The Lagrangian Monte Carlo particle method [7] is widely used to solve the PDF transport equation. In this method, an equivalent particle system is designed to represent the PDF, and the evolution of the particles to represent the evolution of the PDF. For each particle, a set of stochastic differential equations (SDEs) is solved in the physical and composition spaces to account for particle transport, mixing and reaction. Particle tracking and the accurate solution of the SDEs are hence crucial for the success of the methods. In this work, we use LES for the velocity, and PDF for the chemical compositions. The numerical solution of the coupled SDEs arising from the composition PDF method is non-trivial and includes an SDE for particle position and a random ordinary differential equation for compositions. In all previous LES-PDF practice, only first-order accuracy is achieved in integrating the particle equations due to the lack of second-order splitting schemes for the coupled SDEs. Recently, Wang et al. [15] developed several second-order splitting schemes to solve the coupled SDEs more accurately.

In this work, we develop the LES/PDF capability for turbulent combustion. A new PDF code called HPDF has been developed with the following attributes: second-order accuracy in space and time; scalable up to 4096 cores; supporting Cartesian and polar cylindrical coordinate systems; parallelizable by domain decomposition in two dimensions; and it has a general interface to facilitate coupling to different existing LES (or RANS) codes. Here, we link HPDF to an existing LES code [18,19,10] to study a turbulent $\text{CH}_4/\text{H}_2/\text{N}_2$ jet flame (DLR Flame A) [16,17]. In this first publication based on the new code, we address the following issues: the verification of the PDF code, the effect of the LES grid resolution, the consistency between LES and PDF, the sensitivity of the LES results to CFL number, and the performance of different time-integration schemes (first-order and second-order) in HPDF. Comparison is also made with the experimental data [16,17] to show the capability of the LES/PDF code. This study establishes the basis for our future work to consider many species, differential-diffusion, advanced numerical models etc. in LES/PDF.

In this initial study, to address the above issues, we select a flame without strong turbulence/chemistry interactions so that it can be accurately described by a simple combustion model. Accordingly, we make the following simplifications. First, a single laminar flamelet profile is used in both LES and PDF to retrieve density and compositions as functions of mixture fraction. DLR Flame A ($Re = 15200$) exhibits very little local extinction. For this flame, the

flamelet profile is expected to be capable of representing the turbulent non-premixed flame reasonably well. Second, no feedback (primarily density) from PDF to LES is taken into account. We refer to this as one-way coupling. In LES, the transport equations for the mass, the momentum, and the resolved mixture fraction and mixture fraction squared are solved, and the density is obtained from the flamelet profile by presuming a beta-PDF for the SGS fluctuations of the mixture fraction. The velocity, diffusivity, and density obtained from LES are used in the particle transport. The first two moments of the mixture fraction from LES and PDF are mathematically consistent, which provides a useful verification for the PDF code to ensure that the particle operations (particle transport, mixing etc.) are performed correctly and accurately. The density obtained from PDF is computed for output only to compare it with the density from LES. No feedback from PDF to LES takes place in this study. This one-way coupling is adequate for addressing the numerical issues studied in this work. In contrast, two-way coupling would have feedback from PDF to LES in order to obtain density that can be used for the LES solution (and for the particle transport). This two-way coupling between LES and PDF is an important issue which will be addressed in our future work.

LES simulations of DLR Flame A have been performed by Ihme et al. [23] for the study of noise generation. In that study, a flamelet/progress variable combustion model is employed. The numerical results of the resolved mean and rms of the axial velocity, the mixture fraction and the temperature were found to be in very good agreement with the measurement [16,17] at the axial locations $x/D = 10, 20$, and 40. PDF calculations of DLR Flame A in the RANS context have been performed by Lindstedt and Ozarovsky [24]. A reduced reaction mechanism containing 20 species is used in the PDF calculations. Generally, good agreement of the PDF results with the experimental data is observed for the velocity, temperature, and the species mass fractions. No work has been previously reported in the literature based on the LES/PDF approaches for this flame.

2. Computational details

2.1. LES solution

The LES code used in this work is based on [18,19,10]. The LES transport equations for mass, momentum and scalars are cast in a cylindrical-coordinate form for the simulations of the jet flame. The equations are solved using a finite-difference method in the cylindrical-coordinate

system with a structured non-uniform grid and with second-order accuracy in space and time. The pressure projection (or fractional-step method) is used to enforce continuity. The Smagorinsky model with the dynamic procedure is employed to obtain the SGS eddy viscosity μ_{sgs} and diffusivity Γ_{sgs} . Details of the LES solution algorithms can be found in [10,18,19].

The transport equations for the resolved mixture fraction ξ and the resolved mixture fraction squared ξ^2 are solved in LES. The dissipation rate $\tilde{\chi}$ of the residual variance of mixture fraction is modeled as

$$\tilde{\chi} = \Gamma \nabla \tilde{\xi} \cdot \nabla \tilde{\xi} + (\Gamma_{\text{sgs}} + 2\Gamma) \widetilde{\xi'^2} / \Delta^2, \quad (1)$$

where Γ is the molecular diffusivity, $\widetilde{\xi'^2}$ is the residual variance of mixture fraction ($\widetilde{\xi'^2} = \xi^2 - \tilde{\xi}^2$), and Δ is the filter size. The tilde “ \sim ” denotes density-weighted filtering.

A single laminar flamelet profile $\phi = \mathbf{F}(\xi)$ (where ϕ is species mass fractions \mathbf{Y} , temperature T , density ρ , etc.) is used to obtain the compositions, which is obtained from an OPPDIF [20] calculation. The GRI 2.11 mechanism [21] is used to describe the chemical reactions in OPPDIF, and the mixture-averaged formula for diffusion velocities is used to treat molecular transport. A nominal strain rate of $a_n = 100 \text{ s}^{-1}$ is specified for the OPPDIF calculation.

A beta-function PDF is presumed for the SGS mixture fraction fluctuations, and a pre-computed 2D table $\tilde{\phi} = \mathbf{G}(\tilde{\xi}, \widetilde{\xi'^2})$ is created based on the flamelet profile to retrieve resolved species mass fractions $\tilde{\mathbf{Y}}$, temperature \tilde{T} , and density $\tilde{\rho}$ in LES given the solutions of $\tilde{\xi}$ and $\widetilde{\xi'^2}$. The overline “ \sim ” denotes the filtering operation.

The molecular transport properties used in LES are approximated by the following relations, which are obtained from an empirical fit to the laminar flame calculations:

$$\mu/\tilde{\rho} = v_0 (\tilde{T}/T_0)^{1.66}, \quad (2)$$

$$\Gamma = c_0 v_0 (\tilde{T}/T_0)^{1.69}, \quad (3)$$

where $v_0 = 2.22 \times 10^{-5} \text{ m}^2/\text{s}$, $T_0 = 300 \text{ K}$, $c_0 = 1.22$. Thus, $\mu/\tilde{\rho}$ and Γ are taken to depend solely on \tilde{T} .

2.2. PDF methods and particle methods

The composition PDF method accounts for the evolution of the PDF $f(\psi)$ of compositions ϕ explicitly by solving the PDF transport equation. The PDF equation is solved numerically by the particle-mesh method. The LES grid is also used in the PDF code for constructing statistics and performing mixing. The following modeled SDEs for an ensemble of particles are integrated which represent the PDF,

$$d\mathbf{X}(t) = \left[\tilde{\mathbf{U}} + \frac{\nabla[\bar{\rho}(I_{\text{sgs}} + I)]^*}{\bar{\rho}} \right] dt + \left[2(I_{\text{sgs}}^* + I^*) \right]^{\frac{1}{2}} d\mathbf{W}, \quad (4)$$

$$d\phi(t) = -\Omega^*(\phi - \tilde{\phi}^*) dt + \mathbf{S}(\phi) dt, \quad (5)$$

where $\mathbf{X}(t)$ is the particle position, $\tilde{\mathbf{U}}$ is the resolved velocity field, Ω is the scalar mixing frequency, \mathbf{S} is the reaction source term, and the superscript “*” denotes evaluating the quantity at $(\mathbf{X}(t), t)$. The IEM model is used to model the mixing in the scalar Eq. (5).

A simple splitting scheme can be constructed to integrate the SDEs (4) and (5), e.g., $\mathbb{T}^{\text{Euler}}\mathbb{M}\mathbb{R}$ which denotes taking sub-steps of transport \mathbb{T} , mixing \mathbb{M} , and reaction \mathbb{R} in this order each for a time-step Δt . The first-order Euler scheme is used to integrate (4) in this splitting, and overall first-order accuracy is observed for this scheme. Different types of second-order splitting schemes are developed in [15]. In this work, we consider the following type of second-order splitting, $\mathbb{T}^{\text{kp}}\mathbb{M}\mathbb{R}\mathbb{M}\mathbb{T}^{\text{kp}}$, in which \mathbb{T} and \mathbb{M} appear twice to indicate that the transport and mixing are performed twice with time-step size $\Delta t/2$ within each time-step. A second-order SDE scheme KP [22] is used to integrate (4) in this splitting. Details about the second-order splitting for (4) and (5) are given in [15].

The coefficients needed for integrating (4) and (5) (e.g., $\tilde{\mathbf{U}}^*$, I_{sgs}^* , Ω^*) are obtained by interpolating the corresponding LES grid-based fields to the particle locations with simple tri-linear interpolation. A mesh grid identical to the LES grid is used to track the particles and to form the statistics. Ghost cells with particles are used on the inflow/outflow boundary of the computational domain to have the desired particle mass flow rate through the boundary. Algorithms for particle cloning and annihilation are used to ensure an approximately constant number of particles in each cell after each particle transport sub-step, so that sufficient particles are available to form cell ensemble statistics, e.g., the density $\bar{\rho}_p$ and the q th moment of the mixture fraction $\tilde{\zeta}_p^{zq}$ (where the subscript “p” denotes a quantity obtained from the particles to distinguish it from the same quantity obtained from LES). In a given cell containing N particles, these quantities are determined as

$$\bar{\rho}_p = \frac{\sum_{i=1}^N m_i^*}{\sum_{i=1}^N m_i^* v_i^*}, \quad (6)$$

$$\tilde{\zeta}_p^{zq} = \frac{\sum_{i=1}^N m_i^* \zeta_i^{zq}}{\sum_{i=1}^N m_i^*}, \quad (7)$$

where m_i^* , v_i^* , and ζ_i^* are the mass, specific volume and mixture fraction of the i th particle in the cell.

In this work, only a single scalar (mixture fraction) is considered in the scalar Eq. (5). The first two moments $\tilde{\zeta}_p^q$ ($q = 1, 2$) from the particles are consistent mathematically with $\tilde{\zeta}^q$ ($q = 1, 2$) from LES given that the mixing frequency Ω in Eq. (5) is modeled as $\Omega = \tilde{\chi}/\tilde{\zeta}^2$. The laminar flamelet profile $\phi = \mathbf{F}(\xi)$ is used to obtain density, temperature and species mass fractions for particles.

3. Verification of the HPDF code

The new HPDF code is verified for grid convergence and temporal convergence using the manufactured 1D test case described in [15]. Details about the testing are given in [15]. The grid convergence is shown in Fig. 1. The convergence error \mathcal{E} [15] is measured in terms of $\tilde{\zeta}_p$, $\tilde{\zeta}_p^2$, and the particle mass density $\bar{\rho}_p = \sum_{i=1}^N m_i^*/V_{\text{cell}}$, where V_{cell} is the volume of the corresponding grid cell. It is clear from Fig. 1 that (for small Δx) all of the errors are proportional to Δx^2 , thus verifying the second-order spatial accuracy of the HPDF code.

The temporal convergence is shown in Fig. 2 for both the first-order and second-order splitting schemes discussed in Section 2.2. For the first-order splitting scheme (the left sub-plot of Fig. 2), the errors for small Δt are proportional to Δt , which confirms the first-order temporal convergence of the scheme. For the second-order splitting scheme (the right sub-plot of Fig. 2), the errors for small Δt are proportional to Δt^2 , thus verifying the second-order accuracy of the scheme.

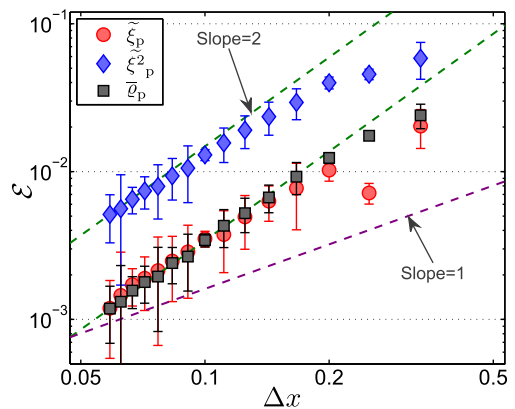


Fig. 1. Numerical error \mathcal{E} as a function of grid spacing Δx for the 1D test of the HPDF code. Circles, mean mixture fraction; diamond, mean mixture fraction squared; squares, mean density; error bars, 95% confidence intervals; dashed lines, reference lines with slope one and two, corresponding to first and second-order spatial accuracy, respectively.

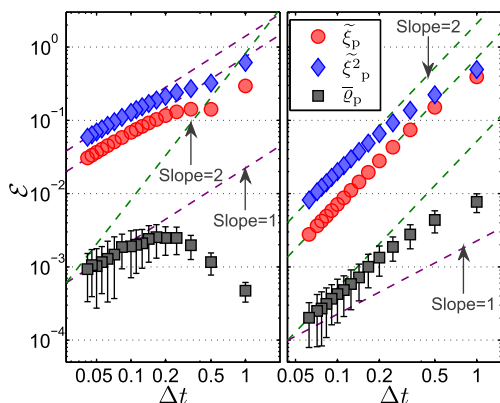


Fig. 2. Numerical error \mathcal{E} as a function of time-step size Δt for the 1D test of the HPDF code (left, first-order splitting scheme; right, second-order splitting scheme). Circles, mean mixture fraction; diamonds, mean mixture fraction squared; squares, mean density; error bars, 95% confidence intervals; dashed lines, reference lines with slope one and two, corresponding to first and second-order temporal accuracy, respectively.

Next we link HPDF with the LES code [18,19,10] and perform the LES/PDF simulations of DLR Flame A.

4. LES/PDF calculations of DLR Flame A

A simple turbulent jet flame of $\text{CH}_4/\text{H}_2/\text{N}_2$ [16,17] at moderate Reynolds number ($Re = 15200$), DLR Flame A, is chosen for the study in this work. The jet nozzle has a diameter of $D = 8$ mm (with bulk velocity $U_0 = 42.2$ m/s) surrounded by a low-velocity air coflow (0.3 m/s). The fuel consists of 22.1% CH_4 , 33.2% H_2 , and 44.7% N_2 by volume. The flame exhibits very little local extinction, and hence is suitable for this study using a single laminar flamelet profile to obtain the thermochemical properties.

The computational domain is specified to be $[0, 120D] \times [0, 30D] \times [0, 2\pi]$ in the axial (x), radial (r) and azimuthal (θ) directions. Three non-uniform grids are used in the simulations, of sizes $64 \times 64 \times 16$, $192 \times 192 \times 48$, and $320 \times 320 \times 80$ in axial, radial, and azimuthal directions. The grids are concentrated near the nozzle in the axial and radial directions. In HPDF, the same computational domain and grid size are used as in LES. The time-step size is determined by a fixed maximum CFL number ($=0.2$) based on the axial direction only, and the same time-step size is used in both LES and PDF. The CFL number is defined as $\text{CFL} = |U|\Delta t/\Delta x + 4\nu_{\text{eff}}\Delta t/\Delta x^2$, where U , ν_{eff} , Δt , and Δx are the axial velocity, effective kinematic viscosity, time-step size, and axial grid size, respectively. The maximum CFL number occurs near the jet exit, where the axial velocity is large and the grid spacing is small. The resulting

time step is relatively small, e.g., $\Delta t \approx 3.3 \mu\text{s}$ for the $192 \times 192 \times 48$ grid. The value of $\text{CFL} = 0.2$ is used for all the results presented below except in Section 4.4 where the sensitivity to time-step size ($\text{CFL} = 0.1, 0.2, 0.5$, and 0.8) is explored.

4.1. Effect of LES grid resolution

We first discuss the time-averaged LES calculations of the flow field in DLR Flame A and their comparison with the experimental data [16,17]. Figure 3 compares the time-averaged radial profiles at the four axial locations $x/D = 5, 10, 20$, and 40 . Time-averaging is denoted by $\langle \cdot \rangle$. The quantities shown are the resolved axial velocity $\langle \tilde{U} \rangle$, the resolved axial turbulence intensity $\langle u'' \rangle = (\langle (\tilde{U})^2 \rangle - \langle \tilde{U} \rangle^2)^{1/2}$, the resolved Reynolds shear stress $\langle u''v'' \rangle = \langle \tilde{U}\tilde{V} \rangle - \langle \tilde{U} \rangle \langle \tilde{V} \rangle$, the resolved mean mixture fraction $\langle \tilde{\xi} \rangle$, and the resolved root mean square (rms) $\langle \xi'' \rangle = (\langle (\tilde{\xi})^2 \rangle - \langle \tilde{\xi} \rangle^2)^{1/2}$. As may be seen from Fig. 3, the results from the two finest grids ($192 \times 192 \times 48$ and $320 \times 320 \times 80$) are almost coincident, with the largest differences being in $\langle u'' \rangle$ at $x/D = 5$. There is striking agreement between these results and the experimental data. In contrast, the results from the coarse grid ($64 \times 64 \times 16$) are significantly different (and in extremely poor agreement with the experimental data). The $192 \times 192 \times 48$ grid seems adequate to capture the flow fields of interest, and hence this grid is used to obtain all the results presented below.

4.2. Consistency between LES and PDF

In this work, the fields of mixture fraction ($\tilde{\xi}$ and $\tilde{\xi}^2$) and density $\tilde{\rho}$ are duplicated in the LES and PDF codes. The evolution equations for the resolved mixture fraction $\tilde{\xi}$ and mixture fraction squared $\tilde{\xi}^2$ used in LES are consistent with those for the first two moments implied by the modeled PDF equation ($\tilde{\xi}^q$, $q = 1, 2$) given the proper modeling of the residual mixture fraction dissipation rate $\tilde{\chi}$ (Eq. 1) and the mixing frequency Ω (modeled as $\Omega = \tilde{\chi}/\tilde{\xi}''^2$) in Eq. (5). Numerically, these results are not the same due to the different numerical errors involved in the LES and PDF codes. It is interesting to see how different these two sets of numerical results are from each other. This mathematical consistency of the mixture fraction field from LES and PDF provides a useful testing for the PDF code. The density field from LES $\tilde{\rho}$, however, is not consistent with the density from PDF $\tilde{\rho}_p$ due to the different probability distribution of SGS mixture fraction used in the LES code (presumed beta-PDF) and in the PDF code (explicitly solved from the PDF transport equation).

In HPDF, 50 particles per grid cell are used, resulting in about 88 million particles in total for

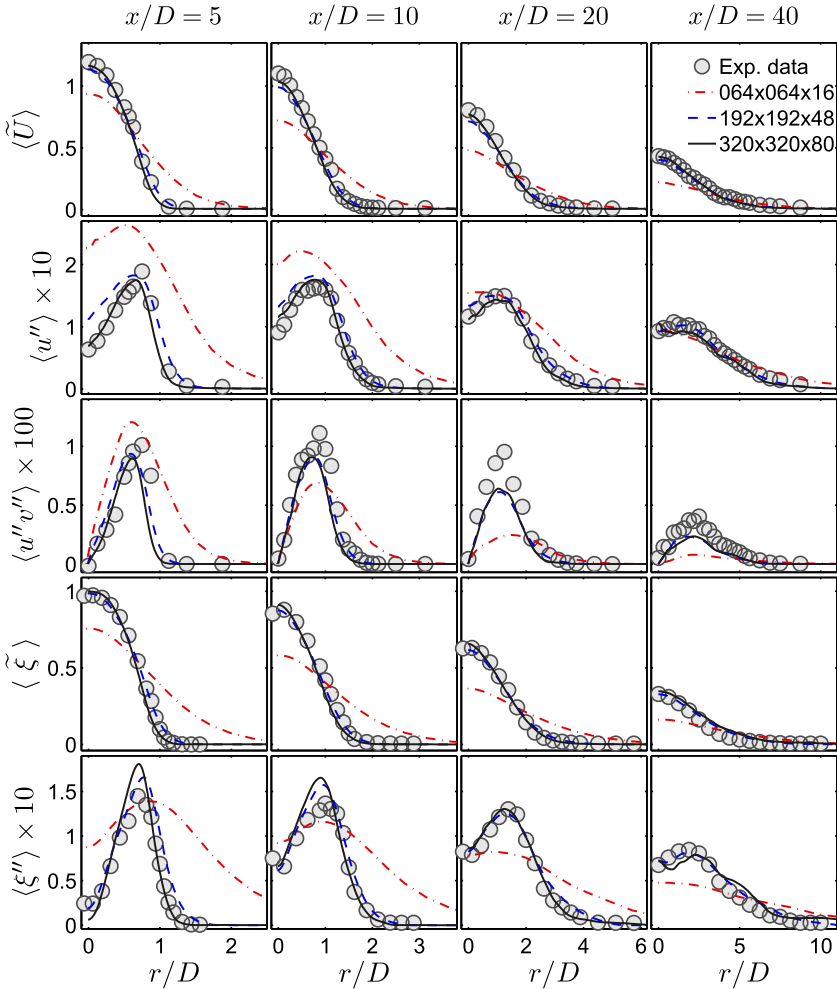


Fig. 3. Radial profiles of the time-averaged axial velocity $\langle \tilde{U} \rangle$, the axial turbulence intensity $\langle u'' \rangle$, the Reynolds shear stress $\langle u'' v'' \rangle$, the resolved mean mixture fraction $\langle \tilde{\xi} \rangle$, and the resolved rms $\langle \xi'' \rangle$ at the four axial locations $x/D = 5, 10, 20$, and 40 . Symbols: experimental data [16,17]; Lines: LES calculations, dash-dotted — $64 \times 64 \times 16$ grid, dashed — $192 \times 192 \times 48$ grid, solid — $320 \times 320 \times 80$ grid.

the grid $192 \times 192 \times 48$. The code starts from existing LES fields in the statistically-stationary state, and initializes the particle properties from the LES fields, e.g., initializing the particle mixture fraction by interpolating the LES field $\tilde{\xi}$ to the particle locations. About 50,000 time steps are marched for the particles to reach the statistically-stationary state. Then, another 50,000 time steps are executed to perform time averaging. The 50,000 time steps correspond to about seven flow through time estimated based on the center-line jet inlet velocity. The second-order time integration scheme $\text{T}^{\text{kp}}\text{MRMT}^{\text{kp}}$ (Section 2.2) [15] for the particle equations (Eqs. (4) and (5)) is used in all the following simulations unless otherwise specified.

In Fig. 4, we compare the radial profiles of $\langle \tilde{\xi} \rangle$, $\langle \xi'' \rangle$, the total rms $\langle \xi'' \rangle_{\text{Total}} = (\langle \tilde{\xi}^2 \rangle - \langle \tilde{\xi} \rangle^2)^{1/2}$,

and the density $\langle \bar{\rho} \rangle$ from LES and PDF at the four axial locations $x/D = 5, 10, 20$, and 40 . Note that the total variance $\langle \xi'' \rangle_{\text{Total}}^2$ consists of two parts: the resolved variance $\langle \xi'' \rangle^2 = \langle (\tilde{\xi}^2) \rangle - \langle \tilde{\xi} \rangle^2$ and the residual variance $\langle \xi'' \rangle_{\text{Residual}}^2 = \langle \tilde{\xi}^2 \rangle - \langle (\tilde{\xi}^2) \rangle$, i.e., $\langle \xi'' \rangle_{\text{Total}}^2 = \langle \xi'' \rangle^2 + \langle \xi'' \rangle_{\text{Residual}}^2$. The calculations of $\langle \tilde{\xi} \rangle$, $\langle \xi'' \rangle$, $\langle \xi'' \rangle_{\text{Total}}$ from LES (solid lines) and PDF (dashed lines) on the same grid $192 \times 192 \times 48$ are slightly different, yet both agree with the experimental data reasonably well. Due to the mathematical consistency discussed above, hypothetically the difference between the LES and PDF predictions on the same grid is caused by the different numerical truncation errors in the different numerical methods. To support this hypothesis, we plot the LES results on a finer grid $320 \times 320 \times 80$ already shown in Figs. 3 and 4

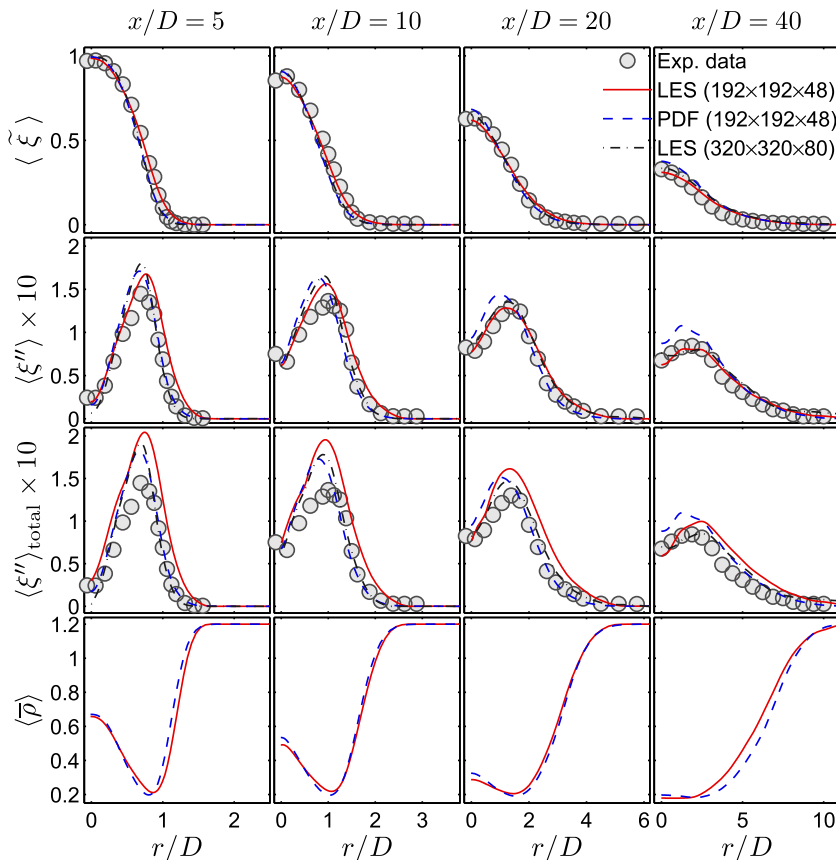


Fig. 4. Radial profiles of the time-averaged mean $\langle \xi \rangle$, the resolved rms $\langle \xi'' \rangle$, the total rms $\langle \xi'' \rangle_{\text{Total}}$, and the density $\langle \bar{p} \rangle$ at the four axial locations $x/D = 5, 10, 20$, and 40 . Symbols, experimental data [16]; solid lines, LES calculations ($192 \times 192 \times 48$); dashed lines, PDF calculations ($192 \times 192 \times 48$); dash-dotted lines, LES calculations ($320 \times 320 \times 80$). (The calculations of $\langle \xi'' \rangle$ and $\langle \xi'' \rangle_{\text{Total}}$ are both compared to the experimental data for $\langle \xi'' \rangle_{\text{Total}}$.)

(dash-dotted lines) for reference. The difference between the LES results on the two different grids is expected to be on the order of Δx^2 where Δx is a nominal grid size for grid $192 \times 192 \times 48$. The difference between the LES and PDF results on the same grid in Fig. 4 is not greater than that between the LES results on the different grids, which suggests that such difference between LES and PDF is on the order of Δx^2 , the expected order of magnitude of the numerical truncation errors in the current simulations. The PDF calculations are in slightly better agreement with the experiments (and with the LES results on the finer grid) than those by LES, e.g., $\langle \xi'' \rangle_{\text{Total}}$ near the jet edge and its peak values at $x/D = 5, 10$ and 20 , which is probably due to the lower spatial truncation errors in the particle method. The percentage of the resolved rms $\langle \xi'' \rangle$ of mixture fraction over the total predicted rms $\langle \xi'' \rangle_{\text{Total}}$ is about 80% near the peak value for the LES results and 95% for the PDF results. This slightly better resolution of the PDF results is probably also due to the lower spatial truncation errors.

The density calculations from LES and PDF are in good agreement as shown in Fig. 4. The slight discrepancy can be explained by the different numerical errors involved in LES and PDF, and by the different probability distribution of SGS mixture fraction in LES and PDF. Recall that in this work, there is no feedback of density from the PDF code, i.e., the density used in the LES code and in the particle transport is from the LES code. The numerical consistency of the density from LES and PDF makes this one-way coupling strategy acceptable for this study.

4.3. Composition fields

In this sub-section, we examine in detail the calculations of the composition fields in DLR Flame A. Figure 5 shows the radial profiles of the time-averaged resolved temperature $\langle \tilde{T} \rangle$, and the resolved mass fractions $\langle \tilde{Y} \rangle$ of CH_4 , O_2 , CO_2 , H_2O , CO , H_2 , OH , and NO at the four axial locations $x/D = 5, 10, 20$, and 40 . Figure 6 shows the

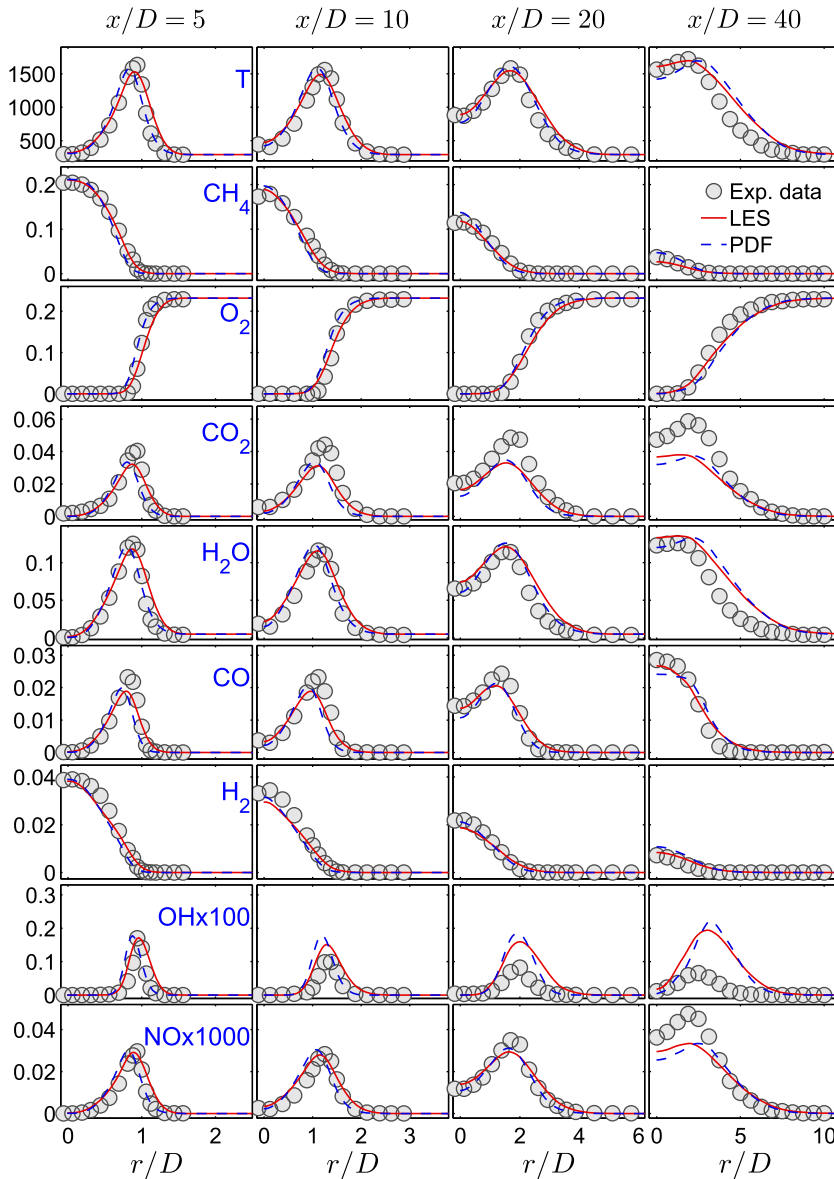


Fig. 5. Radial profiles of the time-averaged mean temperature $\langle \tilde{T} \rangle$, and mean mass fractions of CH_4 , O_2 , CO_2 , H_2O , CO , H_2 , OH , and NO at the four axial locations $x/D = 5, 10, 20$, and 40 . Symbols, experimental data [16]; solid lines, LES calculations; dashed lines, PDF calculations.

time-averaged rms temperature $(\langle \tilde{T}^2 \rangle - \langle \tilde{T} \rangle^2)^{1/2}$ and the time-averaged rms species mass fractions $(\langle \tilde{Y}^2 \rangle - \langle \tilde{Y} \rangle^2)^{1/2}$. These quantities are computed based on the 2D flame table $\tilde{\phi} = \mathbf{G}(\tilde{\xi}, \tilde{\xi}^{n/2})$ in LES and based on the flamelet profile $\phi = \mathbf{F}(\xi)$ in PDF (see Section 2.1). Overall good agreement of the calculations with the experimental data [16] is observed, including for the minor species and NO , largely due to the accurate calculation of the

mixture fraction as shown in Fig. 4. The discrepancy between the calculations and the measurement may be explained by the single laminar flamelet model, which does not account for the effect of fluctuations of the scalar dissipation rate on the flame, and the effect of local extinction. The difference between the LES and PDF predictions is small as expected, given the similar predictions of mixture fraction in LES and PDF shown in Fig. 4.

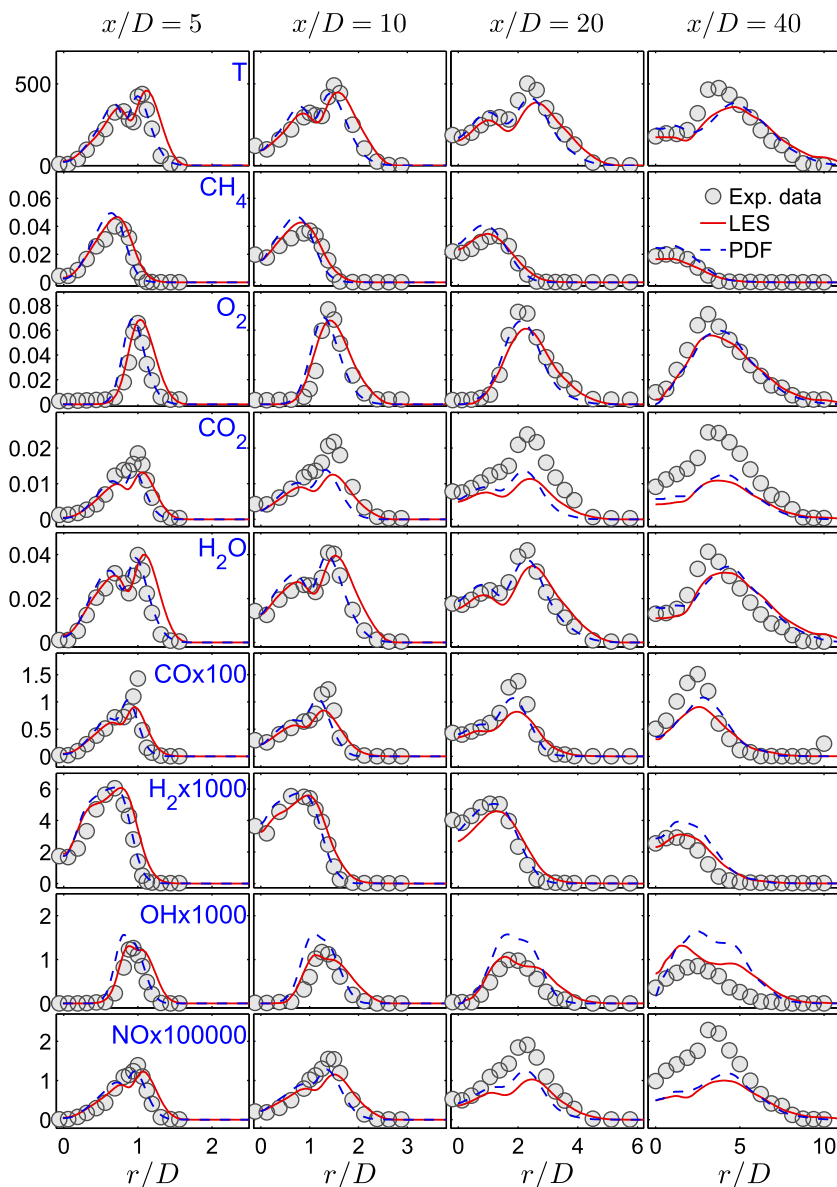


Fig. 6. Radial profiles of the rms temperature, and rms mass fractions of CH_4 , O_2 , CO_2 , H_2O , CO , H_2 , OH , and NO at the four axial locations $x/D = 5, 10, 20$, and 40 . Symbols, experimental data [16]; solid lines, LES calculations; dashed lines, PDF calculations.

4.4. Effect of time-step size and integration schemes

In the results discussed above, a maximum value of $\text{CFL} = 0.2$ is used. Here we vary the maximum CFL number (0.1, 0.2, 0.5 and 0.8) to examine the sensitivity of the LES results to time-step size. The LES results with different maximum CFL numbers are compared in Fig. 7 for $\langle \bar{U} \rangle$, $\langle u'' \rangle$, $\langle u''v'' \rangle$, $\langle \bar{\xi} \rangle$, $\langle \bar{\zeta}'' \rangle$, and $\langle \bar{p} \rangle$ at $x/D = 20$. The results are insensitive to the examined maximum CFL number. For this particular simulation

setup, the axial velocity U decreases and the axial grid size Δx increases along the axial direction. This results in smaller local CFL number in most of the downstream compared to the specified maximum CFL number. The maximum local CFL number from a plane normal to the axis against the axial distance is examined and plotted in Fig. 8 for the specified maximum $\text{CFL} = 0.2$. As can be seen in the figure, the local maximum CFL decreases rapidly in the axial direction, and in the downstream (i.e., $x/D > 20$), the local

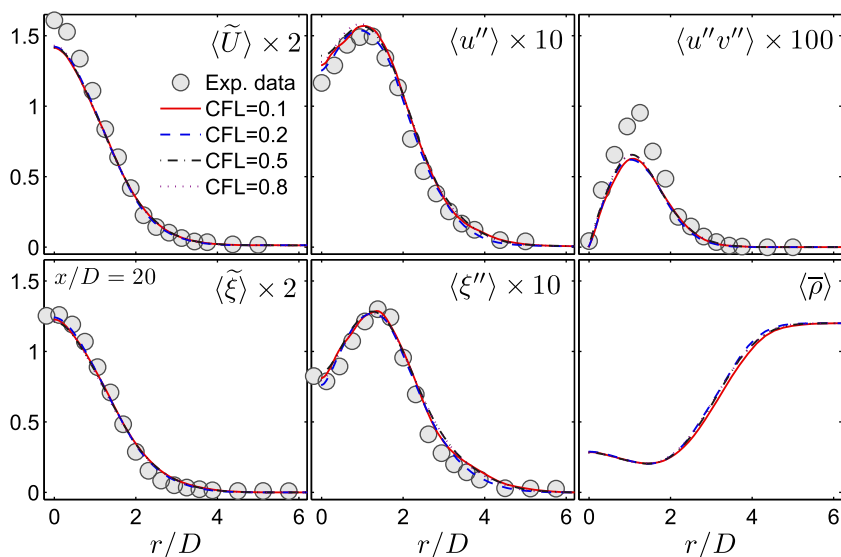


Fig. 7. Radial profiles of the time-averaged axial velocity $\langle \tilde{U} \rangle$, the axial turbulence intensity $\langle u'' \rangle$, the Reynolds shear stress $\langle u''v'' \rangle$, the resolved mean mixture fraction $\langle \tilde{\xi} \rangle$, the resolved rms $\langle \xi'' \rangle$, and the density $\langle \bar{\rho} \rangle$ at $x/D = 20$. Symbols, experimental data [16]; solid lines, LES with CFL = 0.1; dashed lines, LES with CFL = 0.2; dash-dotted lines, LES with CFL = 0.5; dotted lines, LES with CFL = 0.8.

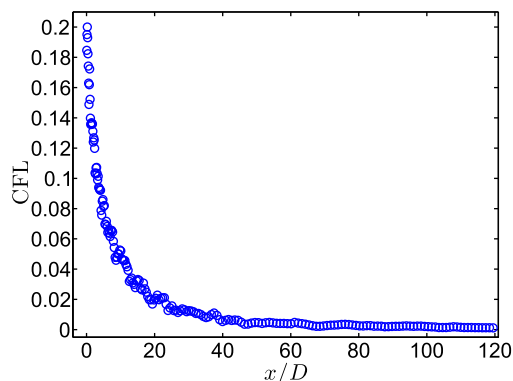


Fig. 8. Maximum local CFL number from a plane normal to the axis against the axial distance x/D for the maximum specified CFL = 0.2.

CFL number is at least one order of magnitude lower than the specified maximum CFL. At the axial distance of $x/D = 20$ where the results are compared in Fig. 7, the local maximum CFL number is about 0.02 which is one order lower than the specified maximum CFL=0.2. Therefore, with maximum CFL of order one, the local temporal discretization error $O(\Delta t^2)$ is two orders of magnitude smaller than the spatial discretization error $O(\Delta x^2)$ for downstream, which can explain why the LES results in Fig. 7 are not sensitive to the maximum CFL number. Due to numerical instability, the maximum CFL number for this

code cannot be increased to greater than one [18,19]. We expect that the spatial discretization error dominates the temporal discretization error for the jet simulations with the current LES code.

In all the previous LES/PDF practices with Lagrangian Monte Carlo particle methods, only first-order temporal accuracy is achieved in integrating the coupled SDEs for particles (Eqs. (4) and (5)) due to the lack of second-order splitting schemes for the SDEs. In this work, a second-order splitting scheme for the SDEs developed in [15] is applied in the simulation of the turbulent jet flame. The performance of the second-order scheme has been shown in [15] and in Fig. 2 for a manufactured 1D test case. The first-order and second-order splitting schemes are further compared in the simulation of DLR flame A in Fig. 9. The first-order splitting scheme is found to be as good as the second-order scheme in predicting the resolved mean $\langle \tilde{\xi} \rangle$, the resolved rms $\langle \xi'' \rangle$, and the density $\langle \bar{\rho} \rangle$. The relative difference of the calculations from these two splitting schemes is within 5%. This small difference is probably due to the fact that the temporal discretization error is dominated by the spatial error so that the differences between the two splitting schemes are not revealed. The first-order splitting scheme seems adequate to evolve the particles accurately for this flame, which is a useful observation because the first-order splitting scheme has only about half of the computational cost of the second-order splitting for the simulations in this work. Meanwhile, this is a valuable

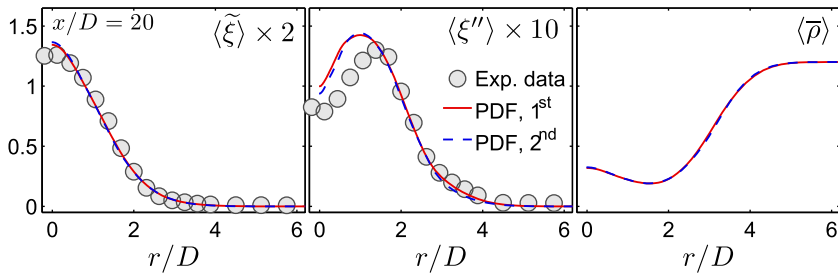


Fig. 9. Radial profiles of the time-averaged mean ($\tilde{\xi}$), the resolved rms (ξ''), and the density ($\bar{\rho}$) at $x/D = 20$. Symbols, experimental data [16]; solid lines, PDF with first-order splitting scheme; dashed lines, PDF with second-order splitting scheme.

conclusion to support the appropriate usage of first-order splitting schemes in all previous LES/PDF practices. This, however, does not suggest that the first-order splitting is adequate for the integration of the particle equations (Eqs. (4) and 5) in all applications of PDF methods. For the simulations of turbulent flows with more uniform local CFL number in the whole computational domain, the temporal truncation errors may be comparable to the other numerical errors, and hence the superiority of the second-order splitting schemes may be evident in those situations like in the test cases in [15] and in Fig. 2.

4.5. Computational cost

We estimate the computational cost of the LES/PDF code for the $192 \times 192 \times 48$ grid with the second-order splitting scheme. About 1.77 million grid cells are used in the LES and PDF. A number of 50 particles per cell is used in HPDF, resulting in about 88 million particles in total. The simulation is performed using 256 cores on the Linux cluster Ranger at the Texas Advanced Computing Center. A 2D domain-decomposition of 64×4 in axial and radial directions is specified in the LES code. A different domain-decomposition strategy is used in HPDF, which optimizes the domain-decomposition automatically by balancing the estimated overall workload (including field operations and particle operations) on each core. The resulting domain-decomposition in HPDF happens to be the same as in LES in this case. The computational cost of the LES/PDF code is about $1600 \mu\text{s}$ per grid cell per time-step. The wall clock time for the code to run for 50000 time steps is about 6.4 days on 256 cores. The cost for the LES part is about $155 \mu\text{s}$ per grid cell per time-step. The HPDF code costs about $26 \mu\text{s}$ per particle per time step. The cost percentage of the HPDF code over the whole code is 90%, i.e., the HPDF cost dominates the LES cost. The parallel scalability of the LES/PDF code depends primarily on the scalability of the HPDF code. We have profiled the HPDF code in a simple 3D

manufactured test case. So far, it is found that HPDF scales well up to 4096 cores for a fixed size problem per core. It is expected that the LES/PDF code scales well up to the same number of cores. More scalability tests will be performed in the future work.

5. Conclusions

In this work, we perform LES/PDF simulations of a turbulent $\text{CH}_4/\text{H}_2/\text{N}_2$ jet flame (DLR Flame A). A manufactured 1D test case is used to verify the convergence of the PDF code, specifically to verify the second-order convergence in space, and the first-order and second-order convergence in time for the first-order and second-order splitting schemes, respectively. Three grids ($64 \times 64 \times 16$, $192 \times 192 \times 48$, $320 \times 320 \times 80$) are used in the simulations to examine the effect of the grid resolution. The numerical results are found to be sensitive to the grid-refinement. The moderate resolution of $192 \times 192 \times 48$ is found adequate to capture the flow fields of interest. The LES and PDF results for the mean and rms mixture fraction and mean density are compared to examine the numerical consistency between LES and PDF. Good agreement between them is observed, suggesting good numerical consistency. Both LES and PDF results are compared with the experimental data. Overall good agreement of the predictions with the experimental data is observed, showing the capability of the employed models to represent the flow and composition fields of this flame. The LES results are found to be insensitive to the maximum CFL number because the local CFL number is much smaller than the maximum specified CFL in the downstream, and the temporal discretization error is mostly dominated by the spatial discretization error. The performance of the first and second-order splitting schemes for the particle equations is compared in the jet flame simulations. For this flame, the first-order splitting scheme performs as well as the second-order splitting scheme in predicting the mean and rms mixture fraction and mean

density. This work establishes the basis for our future work to consider two-way coupling, molecular diffusion, detailed chemistry, other flames etc. in LES/PDF.

Acknowledgments

The authors thank Steven R. Lantz for help with high-performance computing. Helpful discussions with Sharadha Viswanathan, Pavel P. Popov, Konstantin A. Kemenov, David A. Caughey, Venkat Raman and Heinz Pitsch are appreciated. Large parts of the computational results presented in this paper are obtained using the Ranger cluster at the Texas Advanced Computing Center at The University of Texas at Austin. This work was supported in part by Air Force Office of Scientific Research under Grant FA-9550-09-1-0047 and in part it is based upon work supported as part of the Combustion Energy Frontier Research Center funded by the US Department of Energy, Office of Science, Office of Basic Energy Sciences under Award Number DE-SC0001198.

References

- [1] A.W. Cook, J.J. Riley, G. Kosály, *Combust. Flame* 109 (3) (1997) 332–341.
- [2] S. Navarro-Martinez, A. Kronenburg, F. Di Mare, *Flow Turbulence Combust.* 75 (1-4) (2005) 245–274.
- [3] S.H. Kim, H. Pitsch, *Phys. Fluids* 17 (10) (2005) 105103.
- [4] S.B. Pope, *Proc. Combust. Inst.* 23 (1990) 591–612.
- [5] F. Gao, E.E. O'Brien, *Phys. Fluids A* 5 (6) (1993) 1282–1284.
- [6] P.J. Colucci, F.A. Jaber, P. Givi, S.B. Pope, *Phys. Fluids* 10 (2) (1998) 499–515.
- [7] S.B. Pope, *Prog. Energy Combust. Sci.* 11 (1985) 119–192.
- [8] J. Xu, S.B. Pope, *Combust. Flame* 123 (2000) 281–307.
- [9] H. Wang, S.B. Pope, *Combust. Theory Model.* 12 (5) (2008) 857–882.
- [10] V. Raman, H. Pitsch, *Proc. Combust. Inst.* 31 (2) (2007) 1711–1719.
- [11] S. James, J. Zhu, M.S. Anand, *Proc. Combust. Inst.* 31 (2) (2007) 1737–1745.
- [12] M.R. H. Sheikhi, T. G Drozda, P. Givi, S.B. Pope, *Phys. Fluids* 15 (8) (2003) 2321–2337.
- [13] R.O. Fox, *Computational Models for Turbulent Reacting Flows*, Cambridge University Press, 2003.
- [14] S.B. Pope, *J. Fluid Mech.* 652 (2010) 139–169.
- [15] H. Wang, P.P. Popov, S.B. Pope, *J. Comput. Phys.* 229 (2010) 1852–1878.
- [16] W. Meier, R.S. Barlow, Y.-L. Chen, J.-Y. Chen, *Combust. Flame* 123 (2000) 326–343.
- [17] Ch. Schneider, A. Dreizler, J. Janicka, *Combust. Flame* 135 (2003) 185–190.
- [18] C.D. Pierce, *Progress-Variable Approach for Large-Eddy Simulation of Turbulent Combustion*, PhD Thesis, Stanford University, 2001.
- [19] C.D. Pierce, P. Moin, *J. Fluid Mech.* 504 (2004) 73–97.
- [20] A.E. Lutz, R.J. Kee, J.F. Grcar, F.M. Rupley, *OPPDIF: A Fortran Program for Computing Opposed-flow Diffusion Flames*, Report No. SAND96-8243, Sandia National Laboratories, 1997.
- [21] C.T. Bowman, R.K. Hanson, D.F. Davidson, et al. http://www.me.berkeley.edu/gri_mech/.
- [22] P.E. Kloeden, E. Platen, *Numerical Solution of Stochastic Differential Equations*, Springer Verlag, Berlin, 1992.
- [23] M. Ihme, H. Pitsch, D. Bodony, *Proc. Combust. Inst.* 32 (2009) 1545–1553.
- [24] R.P. Lindstedt, H.C. Ozarovskiy, *Combust. Flame* 143 (2005) 471–490.